4-1-2020

Numerical study of roundness effect on flow around a circular cylinder

Ran Wang
University of Windsor

Shaohong Cheng
University of Windsor

David S.K. Ting
University of Windsor

Numerical study of roundness effect on flow around a circular cylinder

Cite as: Phys. Fluids **32**, 044106 (2020); https://doi.org/10.1063/5.0002997
Submitted: 29 January 2020 . Accepted: 01 April 2020 . Published Online: 20 April 2020

Ran Wang, Shaohong Cheng, and David S.-K. Ting

Physics of Fluids ARTICLE scitation.org/journal/phf

Numerical study of roundness effect on flow around a circular cylinder

Cite as: Phys. Fluids 32, 044106 (2020); doi: 10.1063/5.0002997
Submitted: 29 January 2020 • Accepted: 1 April 2020 •
Published Online: 20 April 2020

Ran Wang,[1] Shaohong Cheng,[1,a)] and David S.-K. Ting[2]

AFFILIATIONS

[1]Department of Civil and Environmental Engineering, University of Windsor, Windsor, Ontario N9B 3P4, Canada
[2]Department of Mechanical, Automotive and Materials Engineering, University of Windsor, Windsor, Ontario N9B 3P4, Canada

[a)]**Author to whom correspondence should be addressed:** shaohong@uwindsor.ca

ABSTRACT

Imperfectly round bridge stay cable cross section is speculated to be a key factor for wind-induced large-amplitude cable vibrations observed on site. A delayed detached eddy simulation implemented in Open source Field Operation and Manipulation is used to investigate the flow structure around and in the near-wake of an imperfectly round circular cylinder and the corresponding aerodynamic forces at a Reynolds number of 10^4 and an attack angle of 0° or 45°. With the increase in roundness imperfection, both monotonic and non-monotonic changes of the mean surface pressure and the wake velocity are found when the cylinder is normal to the flow. At an attack angle of 45° and when the roundness ratio is $e/D = 4\%$, it is found that the geometric imperfection in the cross-sectional shape of the cylinder allows it to the retention of more axial flow in the proximity of the cylinder leeward surface due to a shorter recirculation length. The vortex formed by the intensified axial flow would interact with the conventional von Kármán vortex formation at a frequency a few times lower than that of the latter and lead to intermittently amplified transverse lift. This reveals that imperfect roundness in the cross section of a circular cylinder could be an excitation source of low frequency vibration. Thus, it provides evidence that this kind of geometric imperfection, which commonly exists in real stay cables, could contribute to the mechanisms that trigger large-amplitude or even divergent cable motion, such as dry inclined cable galloping on site.

I. INTRODUCTION

Increasing research effort has been dedicated to wind-induced vibrations of stay cables on cable-stayed bridges under no precipitation condition. Owing to the low lateral stiffness, low inherent damping, and light mass, stay cables are sensitive to dynamic excitations such as wind. In typical bridge engineering practice, a high-density polyethylene (HDPE) tube is commonly used to shield a stay cable's steel strands from environmental impact. Thus, a stay cable was modeled as a smooth circular cylinder in many existing experimental[1–3] and numerical[4,5] studies. However, the cross-sectional shape of a real stay cable is not usually perfectly round. Its roundness could be affected by numerous factors including manufacturing precision, assembling processes, and deformations during shipping and storage. For example, Larose *et al.*[6] reported that a deviation of the mean diameter larger than ±5% could exist on site. To clarify the impact of such shape imperfection, researchers prescribed geometric perturbations on a circular cylinder cross section. One of the actively studied topics in fluid mechanics is the groove-shaped geometric perturbation. Large desert plants such as cacti experience high wind velocity in their habitat and evolve a groove-shaped cross section. These organisms provide researchers many new insights into the flow past non-circular bluff bodies.[7,8] Inspired by the groove-shaped cross section, researchers studied[9] the riblet surface aligned in the flow direction, reduced[10] the drag of the base flow in a channel, and optimized[11] a longitudinal groove in a pressure driven flow.

The aerodynamic behavior of a perfectly round circular cylinder has been extensively studied,[5,12] but studies on a cylinder having imperfect roundness are constrained to a limited number of cross sectional shapes, such as 2D arc/triangle groove, pyramid, sand, and emery perturbation.[13] Although this kind of modification on the cross-sectional shape is idealized, it provides many insights into the fundamental problems in fluid mechanics. In the past few years, the roundness effect on the aerodynamic behavior of bridge stay

cables was investigated in the laboratorial environment.[14,15] The results of a wind tunnel test[15] suggested that the imperfect roundness of a circular cylinder could significantly affect drag reduction when the flow is in the critical Reynolds number regime. Furthermore, a wall-resolved large eddy simulation[13] showed that the primary mechanism for the occurrence of drag crisis was not associated with laminar–turbulent boundary-layer transition, but with the interaction between primary flow separation and secondary flow recirculating motions.

In 2015, the Federal Highway Administration Agency (FHWA) of the U.S. initiated a research project to further investigate large amplitude vibrations of bridge stay cables reported in several wind tunnel tests.[2,16] Besides some key parameters, such as the cable inclination angle and the characteristics of atmospheric turbulence, the focus was on the effect of surface irregularities of the HDPE tube. It should be pointed out that this kind of surface imperfection is not identical to the surface roughness but rather indicates the deviation of a cross-sectional shape from the perfectly round one. Insights gained from existing fundamental studies suggested that small imperfection on the cross-sectional shape could have a significant impact on the overall aerodynamic performance of a circular cylinder. Thus, it is reasonable to ask to what extent the imperfection in the cross section roundness would contribute to the aerodynamic instability of a real stay cable.

The wind tunnel test by Wang *et al.*[15] was perhaps the first experimental study attempting to investigate the role of roundness effect in the mechanism of wind-induced large-amplitude cable vibrations without rain. It was observed that compared to a perfectly round circular cylinder, a groove-shaped cross-sectional cylinder has a less significant drag reduction in a lower Reynolds numbers range ($10^5 < \mathrm{Re} < 2 \times 10^5$). However, no sufficient experimental data are available to capture the details of the flow field surrounding the imperfectly round circular cylinder.

In view of this, the current study aims at using delayed detached eddy simulation (DDES) implemented in Open source Field Operation and Manipulation (OpenFOAM version 4.1[17]) to investigate the flow structure around and in the near-wake of a circular cylinder having imperfect roundness and the corresponding aerodynamic forces at a Reynolds number of 10^4 with an attack angle of 0° and 45°, respectively. This would assist us to clarify the possible mechanisms associated with wind-induced large-amplitude cable vibrations under no precipitation conditions on site.

II. NUMERICAL ASPECTS

OpenFOAM is a free, open source software to solve scientific problems in continuum mechanic distributed by the GNU General Public License. It uses a finite-volume method to divide the computational domain into a set of discrete volumes that fill the computational domain without overlap. The equations are then volume-integrated over each individual finite volume using Gauss theorem.

We used the second order scheme, backward, to do the time integration. We used predictor-corrector Pressure Implicit with Splitting of Operators (PISO) to decouple the pressure and velocity fields and solve them iteratively. The velocity matrix system was predicted using the Gauss Seidel solver with a tolerance of 10^{-7}. The pressure matrix system was solved by a geometric agglomerated algebraic multi-grid (GAMG) solver with a tolerance of 10^{-6}. Three PISO correctors were used for each time step.

A. Governing equation and turbulence modeling

The governing equations for the current numerical simulation are the Navier–Stokes equations, where the flowing air is assumed to be incompressible,

$$\nabla \cdot \mathbf{v} = 0, \tag{1}$$

$$\frac{\partial \mathbf{v}}{\partial t} + (\mathbf{v} \cdot \nabla)\mathbf{v} = -\frac{\nabla p}{\rho} + \nu \nabla^2 \mathbf{v}, \tag{2}$$

where $\mathbf{v}$ is the velocity vector, p is the pressure, ρ is the density, and ν is the kinematic viscosity.

A wall-resolved large eddy simulation remains a challenging task for engineering interest.[18] Considering the studied Reynolds number $Re = 10^4$ and the available computational resources, in the current study, we used DDES in OpenFOAM. Menter and Kuntz[19] pointed out that artificial grid induced separation could occur if the switch from Reynolds-averaged simulations (RAS) to large-eddy simulation (LES) takes place and the reduction of eddy viscosity is not balanced by the resolved turbulent content. This "gray area" can occur if the size of the near wall grid is refined to a degree such that the turbulence model switches from RAS to LES contents, but the grid is not fine enough to satisfy the requirement of LES. The modification in the delayed detached eddy simulation improves the "gray area" between RAS and LES. The mathematical details of DDES can be found in our previous work[20] or in the original proposal by Spalart *et al.*[21]

B. Computational domain and boundary conditions

The computational grid has a cylindrical geometry (also known as O-type grid). As shown in Fig. 1(a), the cylinder is located at the center of the computational domain whose diameter and length are $40D$ and $20D$, respectively. A Cartesian coordinate system is used such that the x-axis represents the stream-wise direction, the z-axis coincides with the cylinder axis, and the y-axis is perpendicular to the x-axis and the z-axis. In addition, the attack angle (α) is also denoted in Fig. 1(a).

We adopt a similar definition of roundness used in an earlier wind tunnel study.[15] The cross-sectional shape of the cylinder is formed by superimposing a half-sine curve on one-eighth of a circle. This pattern [denoted by the blue curve in Fig. 1(b)] repeats itself every 45° of axial rotation until the entire cross section is formed. The control variable of roundness is defined as the ratio between the maximum groove depth, e, and the cylinder diameter, D, as shown in Fig. 1(b). This ratio describes the degree of geometric imperfection of a circular cylinder, with $e/D = 0$ corresponding to a perfectly round circular cylinder.

Figure 2 shows the two-dimensional grids of the cylinders with four different roundness ratio cases based on our previous experience.[20,22] Particularly, we selected the two-dimensional grid similar to our previous work.[20] The three-dimensional grid was constructed by extruding the two-dimensional grid along the z-axis. The inlet/outlet planes were half the cylinder surface, as shown

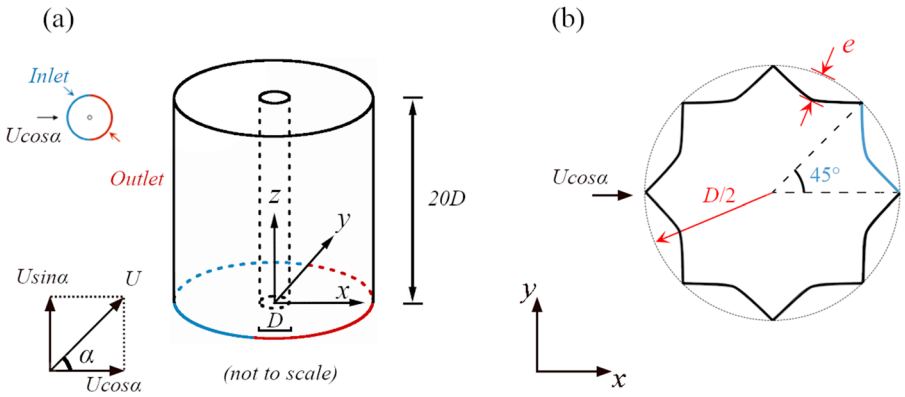

FIG. 1. (a) Sketch of the full computational domain, and (b) illustration of roundness definition.

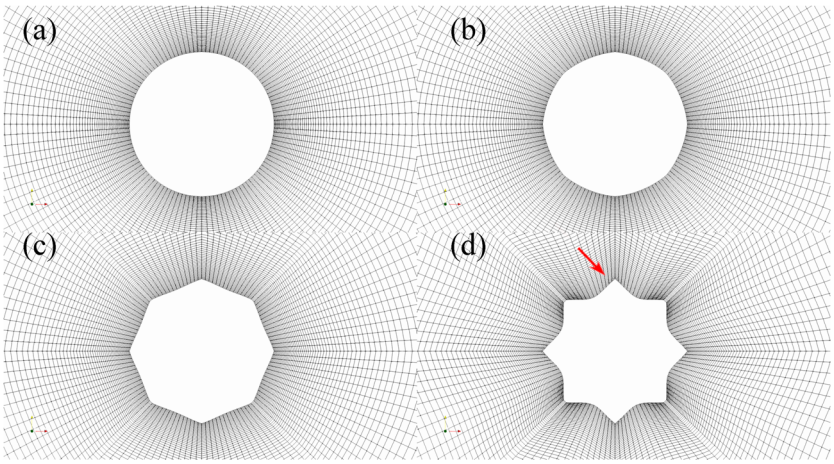

FIG. 2. Mesh details in the vicinity of cylinders with four roundness ratios e/D: (a) 0% (b) 1% (c) 4%, and (d) 10%.

in Fig. 1(a). The following boundary conditions were used in the current study:

- At the inlet plane, a turbulent inlet was adopted of which the corresponding turbulence intensity was around 1%.
- At the outlet plane, a Neumann boundary condition was imposed to the velocities ($\partial u/\partial x = \partial v/\partial y = \partial w/\partial z = 0$) and the pressure was assumed to be zero ($p = 0$).
- On the cylinder surface, a Dirichlet boundary condition for velocities ($u = v = w = 0$) and a zero gradient condition (perpendicular to the cylinder surface) for the pressure were utilized. The turbulent kinematic viscosity was predicted using Spalding's laws to alleviate the extremely fine near-wall resolution near the cylinder surface.
- On the span-wise "wall," the periodic boundary conditions were applied to minimize the end effect.

As indicated in an earlier study,[23] the insufficient size of the computational domain could cause a periodic artifact in the simulation results. Thus, we used a length of $20D$ and 300 layers in the span-wise direction to ensure accurate capturing of the topology associated with the application of the periodic boundary conditions.

A constant time step was chosen to warrant a local Courant number smaller than 1. A non-dimensional time is defined as $t^* \equiv tU_\infty/D$, where t is the dimensional time, U_∞ is the free-stream velocity, and D is the diameter of the cylinder. A summary of the mean drag coefficient, the Strouhal number, and the root-mean-square lift coefficient is given in Table I. The drag and lift coefficients are defined as

$$C_D \equiv \frac{2F_D}{\rho U_\infty^2 DL}, \tag{3}$$

$$C_L \equiv \frac{2F_L}{\rho U_\infty^2 DL}, \tag{4}$$

where F_D and F_L are the total force per unit length in the positive x direction and the positive y direction, respectively, ρ is the air density, and L is the cylinder length. The non-dimensional form of the vortex shedding frequency (f_s) is defined as $S_t \equiv f_s D/U_\infty$. The root-mean-square value of C_L is defined as

$$C_L' \equiv \sqrt{\sum_{n=1}^{N} |C_L(t)|^2/N}, \tag{5}$$

TABLE I. Grid configuration for the normal flow case and the sensitivity study.

Case		Re	L_z/D	N_r (Δr^+)[a]	N_θ $(\Delta\theta^+)$	N_z (Δz^+)	$\overline{C_D}$	S_t	C'_L	$-C_p$	$\lvert u_{min}\rvert/U$	$\overline{L_B}/D$
	Current	1.0×10^4	20	115 (0.004)	118 (0.026)	300 (0.067)	1.14	0.20	0.23	0.96	0.28	1.11
$\alpha = 0°$	Cheng *et al.*[5]	1.0×10^4	3	384	384	96	1.08	...	...	1.20	...	...
	Travin *et al.*[30]	5.0×10^4	2	118	105	30	1.05	0.22	0.21	0.98	...	1.3
	Expt. data	...	...	...	...	...	...	0.21[b]	...	1.10[c]	0.38[d]	1.02[e]
	Coarse	1.0×10^4	20	115	118	200	1.21	0.20	0.21			
$\alpha = 0°$ $(e/D = 4\%)$	Medium	1.0×10^4	20	115	118	300	1.20	0.20	0.17			
	Fine	1.0×10^4	20	115	118	400	1.22	0.20	0.18			

[a]The dimensionless thickness of the near-wall mesh $\Delta r^+ = d/D$, where d is the dimensional thickness and D is the diameter of the cylinder.
[b]From Ref. 24.
[c]From Ref. 31.
[d]From Ref. 32.
[e]From Ref. 33.

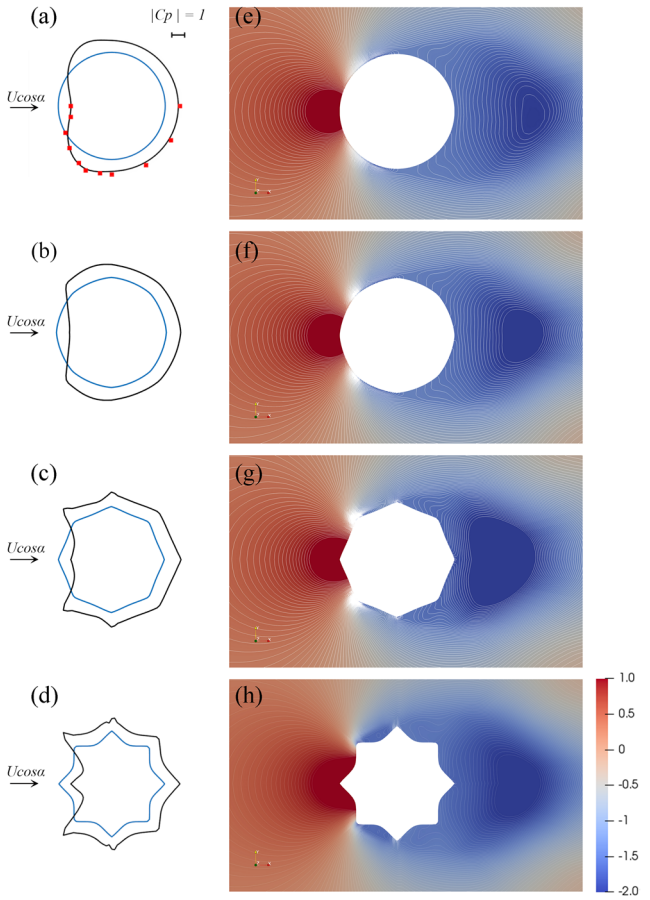

FIG. 3. Mean pressure distribution on the cylinder surface with four roundness ratios e/D at $Re = 10^4$: (a) 0% (red squares are interpolated from Norberg's[25] experimental data), (b) 1%, (c) 4%, and (d) 10%; mean pressure distribution around cylinders: (e) 0%, (f) 1%, (g) 4%, and (h) 10%.

where $C_L(t)$ is the instantaneous lift coefficient. The time averaging process was executed over a period of time corresponding to $T^* = 190$ after the first transitional time period ($T^* = 95$).

C. Validation

The case of the perfectly round circular cylinder not only served as a reference base but was also used for the mesh validation purpose. It can be seen from Table I that the mean drag coefficient of 1.14 obtained from the current numerical model agrees with a wall-resolved LES by Cheng *et al.*,[5] which is $\overline{C_D} = 1.08$ at $Re = 1\times10^4$. The Strouhal number of $St = 0.20$ from the current study at the sub-critical Reynolds number of 10^4 concurs well with the experimental work of Roshko,[24] which reported $St = 0.21$. In addition, the surface pressure distribution around the cylinder is also in general agreement with the experimental data by Norberg,[25] which is shown in Fig. 3(a) as red squares. We also conducted a mesh sensitivity analysis. The computational domain has a span-wise length of $20D$. Three grids, $N_z = 200$, 300, and 400 in the span-wise direction, were tested. The results of a sample case of $e/D = 4\%$ and normal flow condition are given in Table I. It is clear from Table I that further refinement than $N_z = 300$ in the span-wise direction would hardly affect the simulation results. Thus, the grids of other cases in this study were based on the medium grid.

III. RESULTS AND DISCUSSIONS

To explore the impact of imperfect roundness on the flow structure around a circular cylinder and its wake, we simulated flow around circular cylinders having different levels of roundness imperfection when placed normal or inclined to the oncoming flow and compared with the reference case of $e/D = 0$.

A. Attack angle $\alpha = 0°$ (normal flow)

In this section, the flow field and aerodynamic characteristics of circular cylinders having different levels of roundness imperfection, i.e., $e/D = 0\%$, 1%, 4%, and 10%, when exposed to normal flow

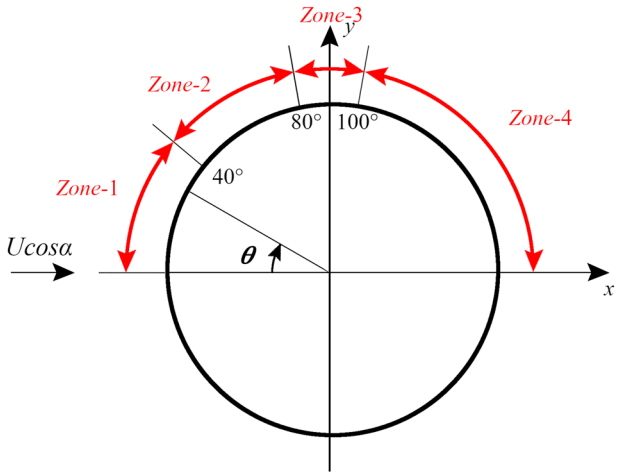

FIG. 4. The angular position of an arbitrary point on the cylinder surface with respect to the stagnation point ($\theta = 0°$) and the locations of zones.

($\alpha = 0°$) are examined. The studied parameters include the surface pressure distribution, the force coefficients, and the wake velocity. The case of $e/D = 0$ is used as the reference base.

1. Surface pressure distribution

Figure 3 illustrates the cylinder surface pressure distribution for four different roundness ratios: e/D = 0%, 1%, 4%, and 10%. The time-averaged pressure coefficient is defined as

$$\overline{C_p} = 2(\tilde{p} - p_0)/(\rho U^2), \tag{6}$$

where U is the oncoming flow velocity, ρ is the air density, $\tilde{p}$ is the time-averaged static pressure on the cylinder surface computed over a non-dimensional time period of $T^* = 190$ after the first transitional time period of $T^* = 95$, and p_0 is the static pressure in the free-stream, which is set to be zero. To better analyze the roundness effect on the surface pressure distribution, we further divide the cylinder surface into four zones, as shown in Fig. 4, based on the observed key features of the surface pressure. The angle, θ, is defined as the angular position of an arbitrary point on the cylinder surface with respect to the stagnation point ($\theta = 0°$), which is used to describe the range of those zones. The positive direction of θ is clockwise. Because of the symmetric distribution pattern of $\overline{C_p}$, only the time-averaged surface pressure distribution in the upper half of the cylinder, i.e., $0° \le \theta \le 180°$, is portrayed in Fig. 5 for the four zones. We choose different scales in different subplots to better illustrate pressure differences in different zones.

Figure 5(a) portrays $\overline{C_p}$ distribution in zone 1, which is the region between the stagnation point ($\theta = 0°$) and $\theta = 40°$ where the cylinder surface is subjected to pressure. Results show that although the cylinder mean surface pressure distribution is marginally affected when the cylinder cross section deviates slightly from the perfectly round shape, as reflected by the fact that the $\overline{C_p}$ distribution in the e/D = 0% and 1% cases is almost identical, with a further increase in e/D, $\overline{C_p}$ increases monotonically, the trend of which is denoted by an arrow in Fig. 5(a). This could be caused by the change in the curvature of the cylinder shape corresponding to different roundness ratios. At larger e/D, the increased curvature could lead to a more considerable change in the surrounding flow direction, which would transfer into more momentum energy, impose larger impulse on the cylinder surface, and result in an increase in surface pressure. Besides, the angular position of the point where $\overline{C_p}$ becomes zero is also found to increase monotonically with e/D. As

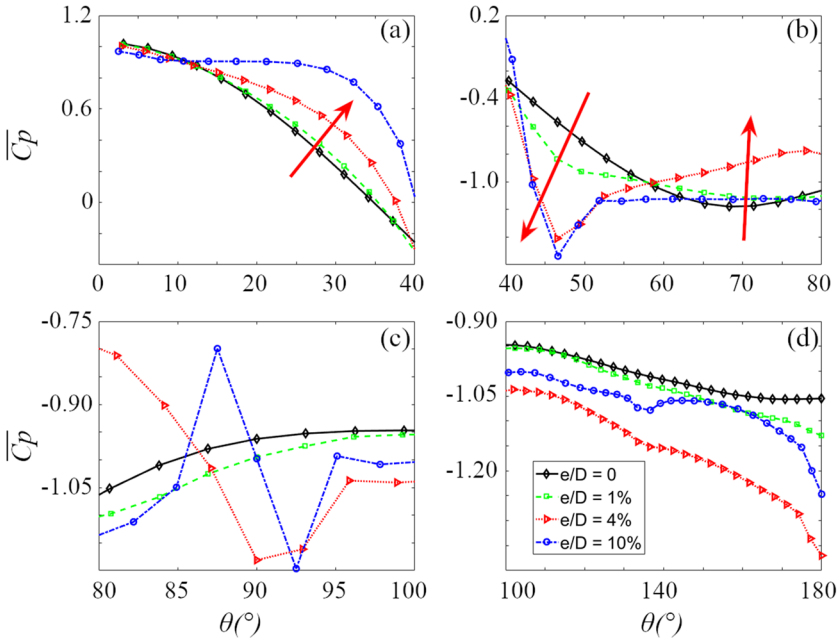

FIG. 5. Pressure coefficient $\overline{C_p}$ details at different angular positions at Re = 10^4—(a) zone 1: $0° \le \theta \le 40°$, (b) zone 2: $40° \le \theta \le 80°$, (c) zone 3: $80° \le \theta \le 100°$, and (d) zone 4: $100° \le \theta \le 180°$.

can be seen from Fig. 5(a), it is 35°, 35°, 38°, and 40° for e/D = 0%, 1%, 4%, and 10%, respectively.

As the flow passes over the beginning region of zone 2 ($40° \le \theta \le 80°$), the surface of the cylinder starts to experience a negative $\overline{C_p}$, i.e., suction, as shown in Fig. 5(b). The decreasing rate of $\overline{C_p}$ is found to be monotonic with respect to e/D increment in the region of $40° \le \theta \le 46°$. The maximum absolute value of the suction, 1.57, is found in the e/D = 10% case. Again, in this region, we found that $\overline{C_p}$ in e/D = 1% follows the pattern of the perfectly round circular cylinder of which the absolute value of $\overline{C_p}$ gradually increases and then slowly decreases. However, when $e/D > 1\%$, a much sharper increase followed by a gradual decrease occurs in the absolute value of $\overline{C_p}$.

Zone 3 ($80° \le \theta \le 100°$) is the region where the flow separates from the cylinder surface in the case of a perfectly round circular cylinder. Again, as can be seen from Fig. 5(c), we found that the $\overline{C_p}$ distribution pattern in the case of e/D = 1% is similar to that of the perfectly round circular cylinder, whereas in the cases of e/D = 4% and 10%, the absolute value of $\overline{C_p}$ shows a sharp increase followed by a decrease in the region $87° \le \theta \le 95°$. Unlike the case of e/D = 4%, where the absolute value of $\overline{C_p}$ continuously increases before θ reaches 90°, in the case of e/D = 10%, the absolute value of $\overline{C_p}$ experiences a sharp reduction when θ changes from 80° to 88°. In addition, although $\overline{C_p}$ increases monotonically toward the leeward side in e/D = 0% and 1% cases, when e/D = 10%, a sudden jump in $\overline{C_p}$ close to the vertex of the cylinder cross section (θ = 90°) can be observed. For example, in e/D = 10%, $\overline{C_p}$ is −1.05 at θ = 85°, it increases to −0.8 at around θ = 88°, and then it drops to −1.2 at round θ = 92°. The geometric location of this sudden jump is denoted by a red arrow in Fig. 2(d). Although the current study only consists of a perturbation of the cylinder surface with eight wavelengths around the cylinder circumference, the trend of this sudden jump agrees with a recent wall-resolved LES by Cheng *et al.*[13] at the location where the cross-sectional shape has a sharp change.

Zone 4 ($100° \le \theta \le 180°$) is on the leeward side of the cylinder. In this region [Fig. 5(d)], the pattern of the $\overline{C_p}$ distribution appears stable. Overall, the absolute value of $\overline{C_p}$ in this region increases as e/D increases. However, it is interesting to find that the minimum $\overline{C_p}$ occurs for e/D = 4% rather than 10%. It can be observed in Fig. 3(c) that the largest suction source on the cylinder leeward side occurs for e/D = 4%, which would be related to the unique flow structure around a circular cylinder with this level of geometric imperfection. This will be further explored in Sec. III B 4.

2. Force coefficient

A summary of the mean drag coefficient, Strouhal number, and root-mean-square of lift of cylinders for the studied cases is listed in Table II. It is found that the Strouhal number, S_t, remains literally unchanged over the range of studied roundness for the normal flow reference case. The current calculated mean drag coefficient ($\overline{C_D}$ = 1.14) and Strouhal number (S_t = 0.20) match well with the experimental data ($\overline{C_D}$ = 1.12 and S_t = 0.20) by Schewe[26] in the subcritical Reynolds number range. A slight discrepancy in $\overline{C_D}$ is observed for different roundness ratios. In particular, $\overline{C_D}$ for the e/D = 4% case is about 5% larger than that of the perfectly round circular cylinder. It should be pointed out that the cross-sectional geometry of the cylinder in the e/D = 4% case is the same as the one studied in a recent wind tunnel test by Wang *et al.*[15] They tested a range of Reynolds numbers from $Re = 5 \times 10^4$ to 4.5×10^5, which covers the sub-critical and critical Reynolds number regimes. The wind tunnel tested was conducted in a closed atmospheric facility with a turbulence level of 0.14% in an empty test section. The tested cylinder had a diameter of 0.09 m and an aspect ratio of L/D = 20. They reported a minor difference of 2% in the $\overline{C_D}$ value between the tested cylinder (e/D = 4%, $\overline{C_D}$ = 1.05) and the perfectly round circular cylinder (e/D = 0, $\overline{C_D}$ = 1.07). It should be pointed out that $\overline{C_D}$ in the e/D = 4% case is larger than that in the e/D = 0 case from the current numerical study, whereas the data in the experimental study by Wang *et al.*[15] showed that $\overline{C_D}$ in e/D = 4% was 2% smaller than that in the perfectly round cylinder. Due to the fact that the relative difference of $\overline{C_D}$ between cases of e/D = 4% and e/D = 0 is rather small, this difference might be attributed to many factors, such as the Reynolds number, the turbulence intensity, and/or the turbulence model used in the current study. In addition, we found that the perfectly round circular cylinder has the highest value of C_L', and the case of e/D = 1% has the lowest value of C_L' in each attack angle case. From the calculated data, it seems that C_L' will first decrease and then gradually increase, when e/D changes from 0% to 10%.

TABLE II. Mean drag coefficient, Strouhal number, and root-mean-square of lift for the studied cylinders with/without roundness at attack angles α = 0° and 45°.

Attack angle α	Roundness ratio e/D	$\overline{C_D}$	St	C_L'
0°	0	1.14	0.20	0.23
	1%	1.10	0.20	0.13
	4%	1.20	0.20	0.17
	10%	1.19	0.22	0.22
45°	0	0.51	0.15	0.07
	1%	0.50	0.15	0.02
	4%	0.55	0.15	0.05
	10%	0.57	0.15	0.04

Figure 6 depicts the time history of the lift force coefficient and their corresponding power spectra. The oscillating feature of lift, which is observed in all four roundness ratio cases, implies the presence of a periodic transverse excitation on the cylinder. However, their corresponding power spectra almost peak at the same frequency. This is possibly due to the same projection area and the relatively small variation of the cylinder cross section. The associated flow structure will be discussed further in Sec. III B 4.

3. Wake velocity

To study how imperfect roundness would influence the near-wake flow structure of a circular cylinder, the variation of the normalized time-averaged streamwise velocity, $\overline{U}/U_\infty$, along the wake centerline is portrayed in Fig. 7, where $\overline{U}$ is the streamwise velocity and U_∞ is the oncoming flow velocity. The normalized recirculation length, L_B/D, where L_B is the distance between the cylinder base point and the location along the centerline where the streamwise velocity changes from negative to positive, is found to be 1.11 for the perfectly round circular cylinder (e/D = 0). A general decreasing trend can be observed of the normalized recirculation length with increasing e/D. The values of L_B/D are 0.92, 0.85, and 0.93 for e/D = 1%, 4%, and 10%, respectively.

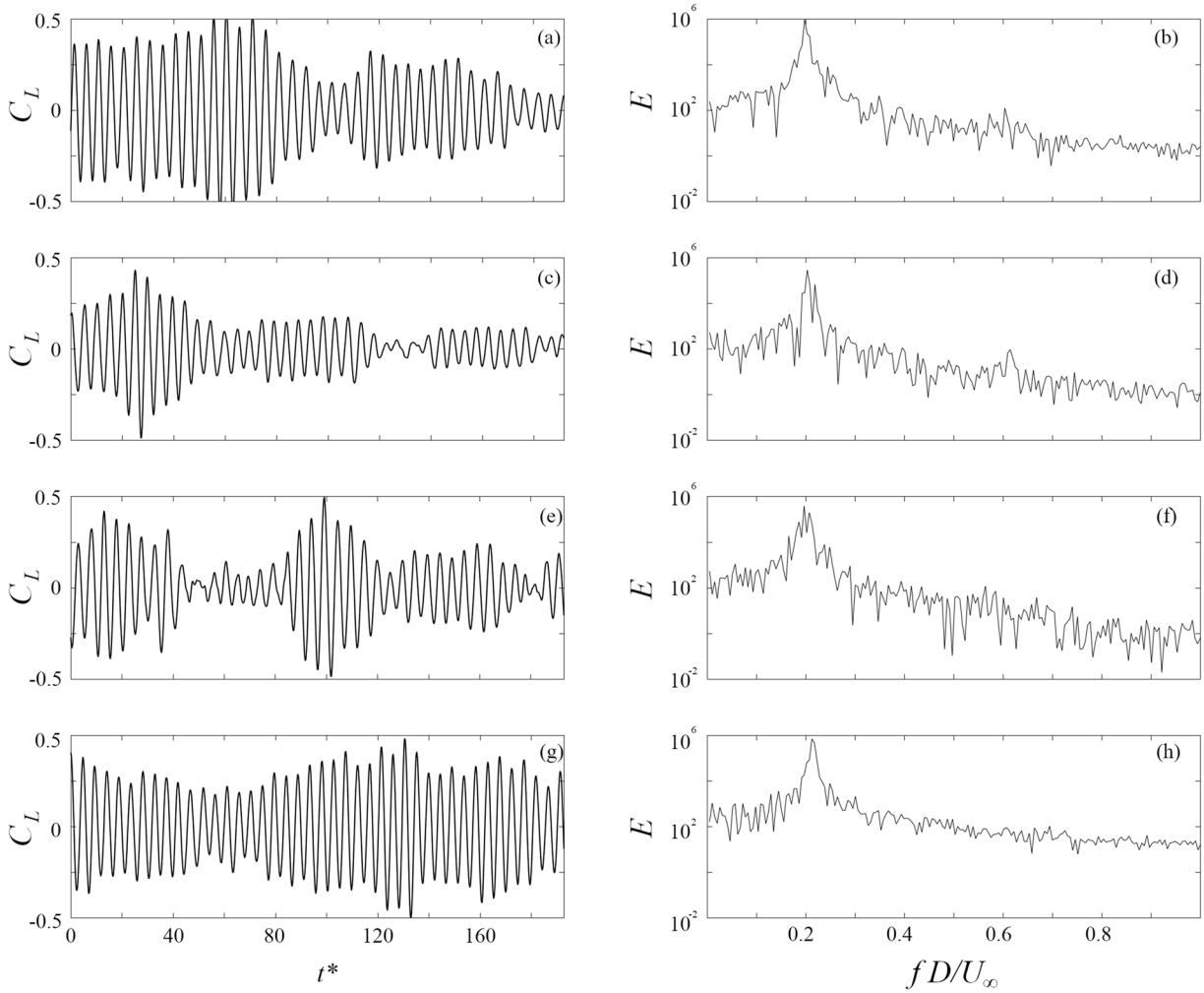

FIG. 6. Time history of span-wise averaged lift coefficient and corresponding power spectra E for different roundness ratios e/D at $Re = 10^4$: [(a) and (b)] 0%, [(c) and (d)] 1%, [(e) and (f)] 4%, and [(g) and (h)] 10%.

To further examine the velocity field within the recirculation bubble, the wake field shown in Fig. 7(a) is divided into three regions, covering the normalized downstream distance x/D from 0.50 to 0.55, 0.55 to 1.60, and 1.6 to 8.0, respectively. It is observed that for all the imperfect roundness cases, the velocity field near the base point (x/D = 0.5) is different from that of the perfectly round circular cylinder case. Figure 7(b) shows that for a circular cylinder having roundness imperfection, the velocity field near the base point is positive, indicating that the flow is moving toward the downstream direction. This is opposite to the case of the perfectly round circular cylinder. In the wake region ($0.50 \le x/D \le 0.55$), the maximum velocity is found to increase monotonically from 0.0027 to 0.1111 with increasing roundness from e/D = 1% to 10%. Figure 7(c) shows the normalized time-averaged streamwise velocity in the middle part of the recirculation zone where the normalized downstream distance is within the range of 0.55 to 1.6. In this region, the streamwise velocity gradually reaches its minimum value and then increases to zero. The e/D = 4% case is found to have the minimum $\overline{U}/U_\infty$ of −0.3. It is worth noting that a negative value of $\overline{U}/U_\infty$ means opposite flow direction with respect to the oncoming flow. In our study, this minimum value of $\overline{U}/U_\infty$ is not found in the case of e/D = 10%. This indicates that the influence of circular cylinder roundness has a nonlinear effect on the flow in the wake region. Another example of this nonlinear relation is the length of recirculation zone, L_B/D. We found that L_B/D decreases from 1.11 to 0.92 when the roundness ratio increases from 0% to 1%. L_B/D further decreases to a minimum value of 0.85 when the roundness ratio is 4%. However, when the roundness ratio further increases to 10%, L_B/D ceases to decrease but instead increases to 0.93. Figure 7(d) shows the time-averaged streamwise velocity distribution in the far-wake region ($x/D > 1.6$). In this region, the magnitude of velocity approaches asymptotically to a constant value. It can be observed that in this region, the

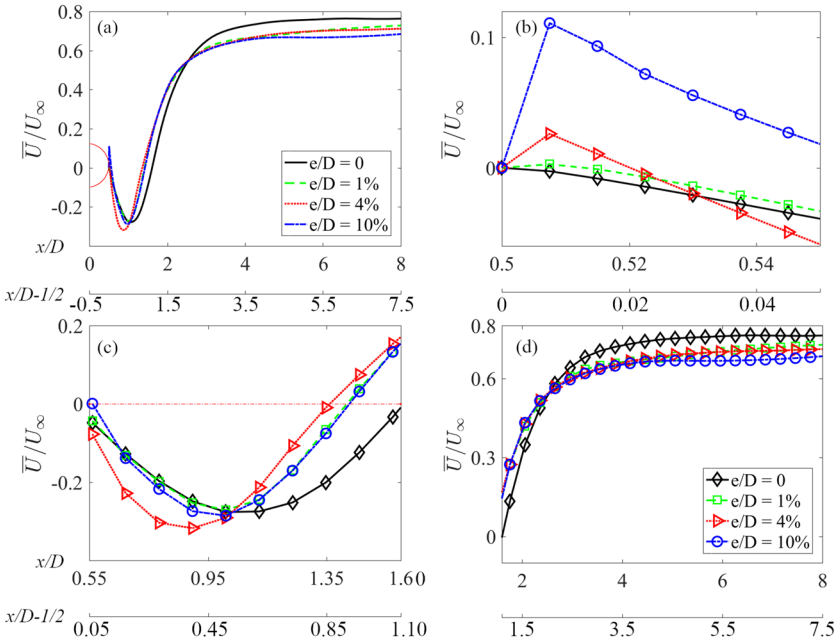

FIG. 7. Time-averaged stream-wise velocity along the wake centerline for the cylinder with four different roundness in different wake regions: (a) overall distribution, (b) $0.50 \le x/D \le 0.55$, (c) $0.55 \le x/D \le 1.60$, and (d) $1.60 \le x/D \le 8.0$. The secondary axes in each subplots measure the distance between the base point and the measured locations.

magnitude of the streamwise velocity of a perfectly round circular cylinder is always higher than that of the imperfectly round ones, indicating that the roundness effect can propagate far into the wake region.

To this point, the roundness effect in the normal flow case has been studied, some monotonic and non-monotonic changes in the cylinder surface pressure distribution have been observed. The wake velocity profiles also show this consistency and inconsistency due to the roundness effect. In Sec. III B, the flow field around and flow-induced forces on an imperfectly round circular cylinder exposed to the flow with an attack angle of 45° will be further investigated.

B. Attack angle α = 45°

Flow around a circular cylinder at normal incidence has been extensively investigated by researchers. Cases of a cylindrical body exposed to flow at a non-zero attack angle are also commonly encountered in engineering practice. Therefore, in this section, the flow field around and aerodynamics associated with circular cylinders having the same four levels of roundness, i.e., e/D = 0%, 1%, 4%, and 10%, when subjected to oncoming flow at an attack angle of 45°, will be further studied for $Re = 10^4$. Both the spatial and temporal variation of the lift force and the near-wake flow structure will be examined in detail.

1. Sectional force coefficient

Figure 8 depicts the contour of the sectional C_L for e/D = 0%, 1%, 4%, and 10% at $Re = 10^4$ when the attack angles are 0° and 45°, respectively. The definition of the sectional C_L is similar to Eq. (4), except that F_L and L are the sectional force and the length of the section, respectively, over which C_L is calculated. The horizontal axis represents the non-dimensional time, t^*. The vertical axis defines the dimensionless span-wise location of the section L_Z/D, where L_Z is the z-coordinate. To better scrutinize the flow structure, we continue the simulation for a non-dimensional time period of $T^* = 154$ after $t^* = 291$.

Overall, the presence of the von Kármán vortex shedding can be recognized from the periodic pattern of the yellow (or red) and cyan (or blue) stripes in Fig. 8. These yellow/cyan (or red/blue) stripes can be used to identify the direction of the lift force acting on the cylinder surface. For example, the yellow (or red) region in the contour means that the cylinder is subjected to a positive lift force, i.e., the lift force is along the positive y-axis [Fig. 1(a)], whereas the cyan (or blue) region represents a negative lift force. The yellow/cyan (or red/blue) stripes in Figs. 8(a), 8(c), 8(e), and 8(g) show a similar pattern as those in Figs. 11(a), 11(e), and 11(g) of our previous study,[20] where these yellow/cyan (or red/blue) stripes are mostly perpendicular to the horizontal axis t^* in the contour of the sectional C_L in both studies. This phenomenon indicates that the flow structure is synchronized over the entire cylinder span. It should be noted that the cylinder studied in the previous work[20] is a perfectly round one. The similarity in the contour of the sectional C_L between the two sets of results suggests that the roundness has negligible impact on the synchronization of the von Kármán vortex shedding over the entire cylinder span in the normal flow (α = 0°) condition. However, it becomes complex when the flow approaches the cylinder at a non-zero attack angle. When the attack angle is at α = 45°, the contour of the sectional C_L shows two distinct features. The first noticeable feature is that the yellow/cyan (or red/blue) stripes start to tilt in the $t^* - z$ domain when e/D = 1% and 4% [Figs. 8(d) and 8(f)], whereas those in the perfectly round case [Fig. 8(b)] are still normal to the horizontal axis $t*$. Interestingly, when e/D = 10% [Fig. 8(h)], the tilt pattern of the yellow/cyan (or red/blue) stripes is found to only roughly exist until $t^* = 340$. For example, the red/blue stripes

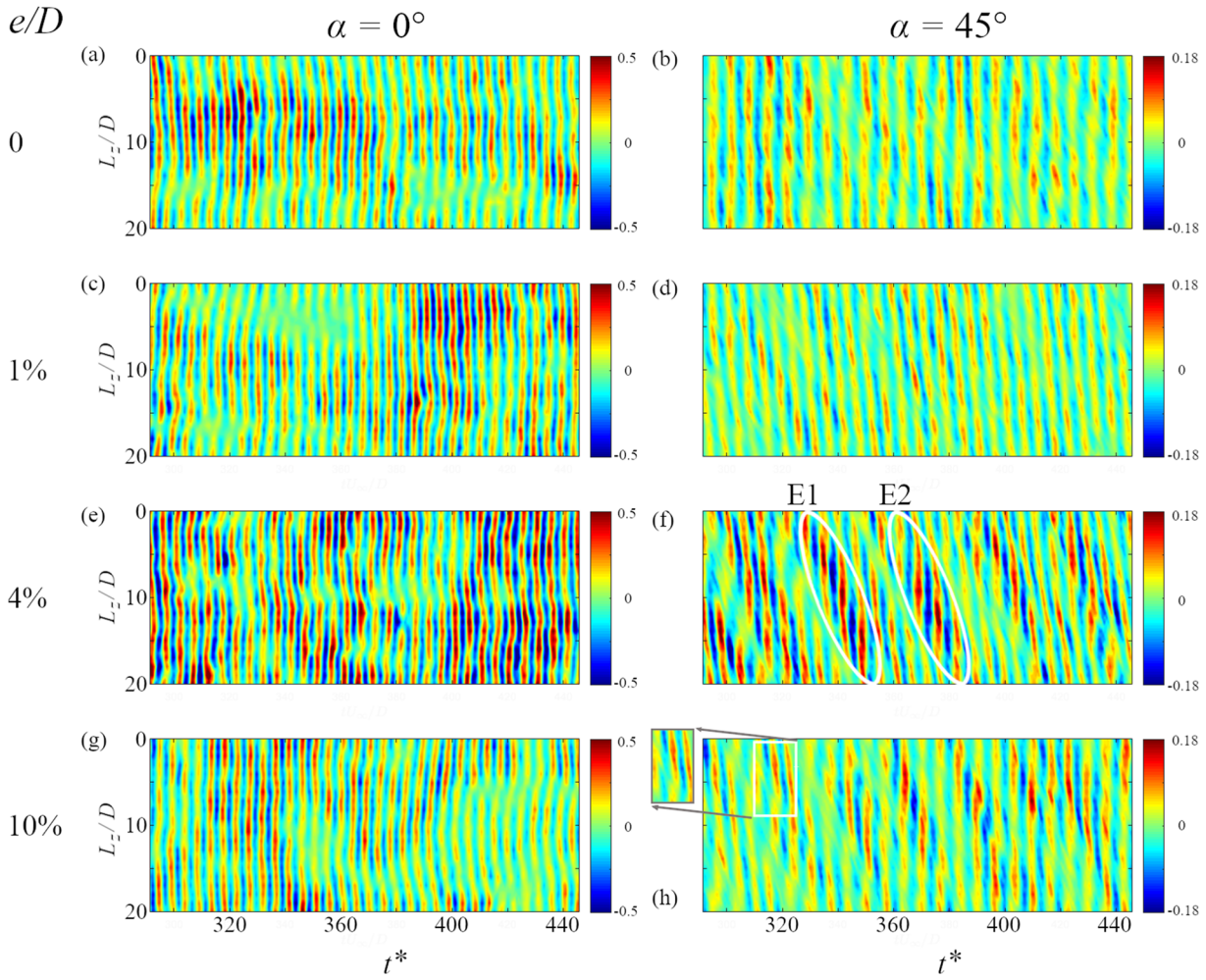

FIG. 8. Sectional lift coefficient contours along the z-axis and time domain for an attack angle of 0°: (a) e/D = 0%, (c) e/D = 1%, (e) e/D = 4%, and (g) e/D = 10%; and for an attack angle of 45°: (b) e/D = 0%, (d) e/D = 1%, (f) e/D = 4%, and (h) e/D = 10% at Re = 10^4.

clearly display this tilt pattern, as shown in the zoomed-in view [left to Fig. 8(h)], at $t^* \approx 320$. Beyond that, the stripes become normal to the t^*-axis again. The second feature is that the magnitude of the sectional C_L exhibits a moving pattern with the larger C_L value gradually traveling from the lower part ($z = 0 - 10D$) of the circular cylinder to the upper part ($z = 10 - 20D$). It should be pointed out that the color in Fig. 8 represents the value of the sectional C_L. Based on the color map, the red/blue represents a larger absolute value of C_L than that of yellow/cyan, so the red/blue stripes in Fig. 8 characterize the localized maximum/minimum lift. This can be clearly distinguished from the case of e/D = 4% shown in Fig. 8(f). A similar moving pattern of the red/blue stripes has also been observed in our previous study[20] for a perfectly round circular cylinder, but at $Re = 1.4 \times 10^4$ and at an attack angle of 30°. Based on the simulation results, we speculate that the geometric imperfection in the cross-sectional shape of a circular cylinder could disturb the separated flow in a similar way as the combined effect of the Reynolds number and the attack angle. With a further increase in e/D from 4% to 10%, this moving pattern of red/blue stripes becomes much less obvious. As shown in Fig. 2(d), when e/D = 10%, the cross-sectional shape of an imperfectly round circular cylinder has relatively deep grooves, which could possibly trap the axial flow and affect the formation of the moving pattern.

The sectional lift force coefficient contour shown in Fig. 8 elucidates much more details about the spatial and temporal variations of the aerodynamic forces than a single mean force coefficient measurement, e.g., C_L or S_t. It is important to point out that this red/blue stripe moving pattern is extremely sensitive to small perturbations. Thus, if we view one set of moving red/blue stripes as one bundle, e.g., the one enclosed in a white elliptical ring E1 ($320 < t^* < 360$) or a white elliptical ring E2 ($360 < t^* < 400$), the existences of these bundles do not always show an organized pattern, as illustrated in Fig. 8(f). Instead, we found that this pattern has a strong irregular intermittent characteristic that the time interval between the two

successive bundles varies from $T^* = 35$ to $T^* = 70$ under the same conditions. A notable example of this is the time lag between two bundles in Fig. 13(a). The reason could be attributed to factors such as turbulence intensity, boundary condition, and even round-off errors.

2. Cross correlation

To characterize the moving pattern of the red/blue stripes shown in Fig. 8(f), we calculate the cross correlation function between the sampled time series of C_L at five span-wise locations. The z-coordinates of these five locations (Z_i, $i = 1$ to 5) are $4D$, $8D$, $11D$, $13D$, and $14D$. A non-dimensional distance S_{ij} between the two adjacent span-wise locations (Z_i and Z_j) is defined as

$$S_{ij} = \frac{Z_j - Z_i}{D} (i = 1 \text{ to } 4, j = i + 1). \tag{7}$$

The cross correlation of C_L between the two span-wise locations Z_i and Z_j is defined as

$$R_{ij} = E[C_{L_i}(t) C_{L_j}(t + \tau)], (i = 1 \text{ to } 4, j = i + 1), \tag{8}$$

where $C_{L_k}(t)$ is the time history of C_L at the span-wise location Z_k [k follows the same index rule in Eqs. (7) and (8)], τ is the time lag, and E is the mathematical expectation.

Figures 9(b), 9(d), 9(f), and 9(h) show the cross correlogram of C_L for a circular cylinder at $Re = 10^4$ with four different levels of roundness imperfection, i.e., $e/D = 0\%$, 1%, 4%, and 10%, when the attack angle is 45°. In addition, we also include the cross correlogram of C_L of the same four circular cylinders when the attack angle is 0° in Figs. 9(a), 9(c), 9(e), and 9(g) for comparison. It can be seen in Fig. 9(a) that when a perfectly round circular cylinder is placed normal to the flow, the C_L cross correlation coefficient R_{ij} would reach a local maximum roughly every non-dimensional time period of $T^* = 6.8$ (or every dimensional time period of $T = 0.36612$ s) for all four studied S_{ij} cases. Given that the cylinder diameter is $D = 0.09$ m and the oncoming flow velocity is $U = 1.67$ m/s, we can estimate the non-dimensional frequency, $St = D/(TU) = 0.1475$. This agrees very well with the result of $St = 0.1490$ determined based on the

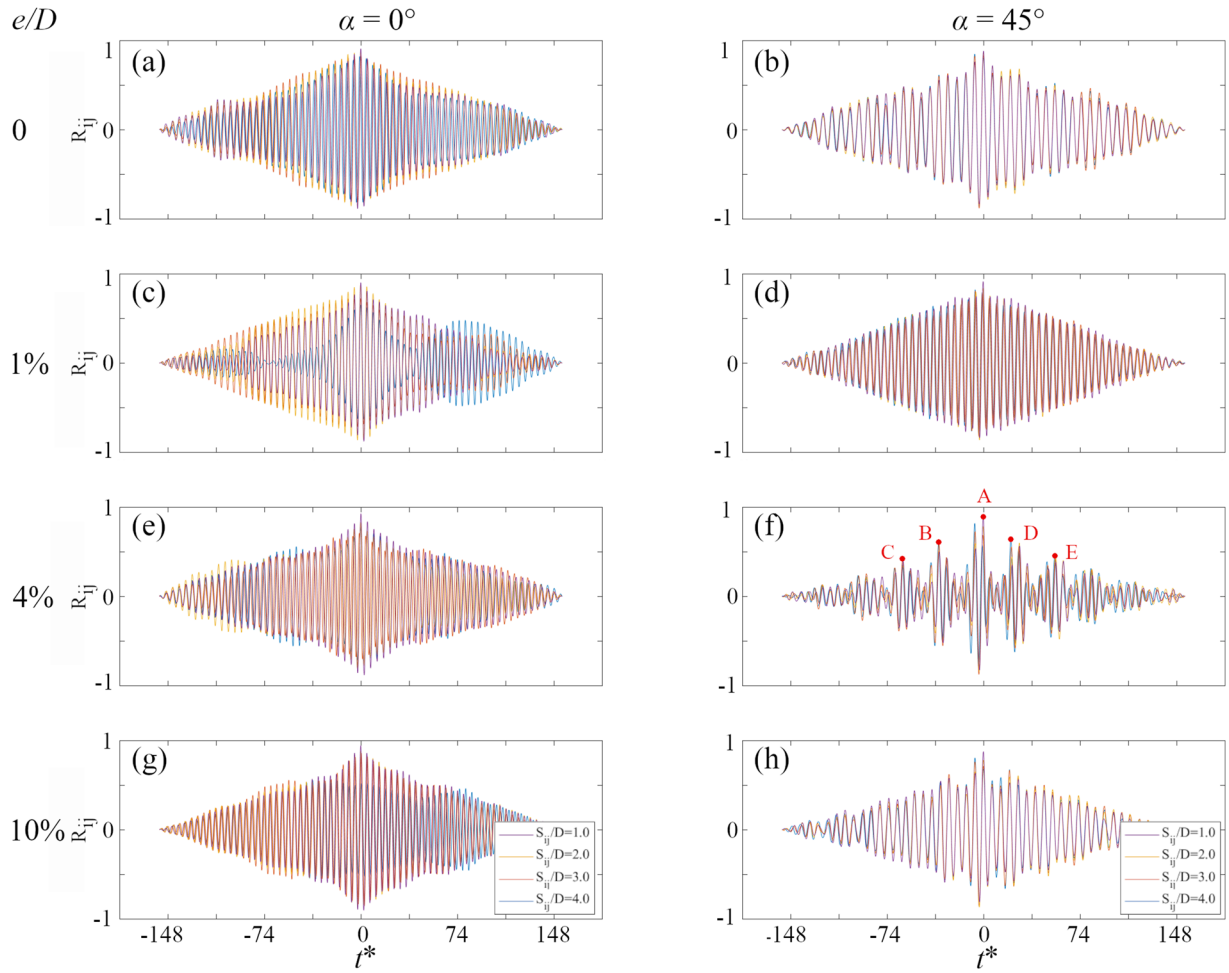

FIG. 9. Cross correlogram of sectional C_L: (a) $e/D = 0\%$, (c) $e/D = 1\%$, (e) $e/D = 4\%$, and (g) $e/D = 10\%$; and for an attack angle of 45°: (b) $e/D = 0\%$, (d) $e/D = 1\%$, (f) $e/D = 4\%$, and (h) $e/D = 10\%$ at Re = 10^4.

span-wise averaged C_L. However, when the attack angle is 45°, although as shown in Table II, the Strouhal number of the e/D = 4% and e/D = 0 cases is the same, the sectional C_L contour of these two cases are found to exhibit considerably different patterns, which are portrayed in Figs. 8(b) and 8(f), respectively.

From the cross correlogram of C_L in Fig. 9(f), it can be observed that, besides the high frequency oscillation related to the von Kármán vortex shedding, a relatively low frequency fluctuation also exists, which amplifies the high frequency peaks once every few cycles. Five typical amplified R_{ij} are denoted by red dots and labeled A, B, C, D, and E in Fig. 9(f). We found that the time interval between any two adjacent red dots is closely related to the second feature, i.e., the moving pattern of the magnitude of the sectional C_L discussed in Fig. 8(f).

It is worth pointing out that based on the existing experimental studies[3,16] and a field record,[27] one of the distinctive response characteristics of a wind-induced divergent type of bridge stay cable vibration, i.e., dry inclined cable galloping, is the low frequency oscillation compared to that induced by the von Kármán vortex shedding. Therefore, it is speculated that although the current numerical results are obtained by assuming a stationary condition of the cylinders, this low frequency amplification pattern of the lift identified in Fig. 8(f) for an imperfectly round circular cylinder (e/D = 4%) at an attack angle of 45° and a Reynolds number of 10^4 could be a potential excitation source, which might lead to an aerodynamic instability of a cable and result in a large amplitude or even divergent oscillation of cables, such as dry inclined cable galloping.

3. Sectional C_p contour

To further study the spatial flow structure inferred from Fig. 8(f), the instantaneous surface pressure distribution on the cylinder for the case of e/D = 4% at an attack angle of 45° and $Re = 10^4$ is examined. The definition of the instantaneous C_p is similar to Eq. (6), except that $\tilde{p}$ is replaced by the instantaneous static pressure. Figure 10 shows the distribution of instantaneous surface pressure by unfolding the cylinder surface. The x-axis represents the angular position of an arbitrary point along the circumference of the cylinder, whereas the y-axis represents the span-wise position of the point. The surface pressure distribution at six time instants, $t^* = 565$, 569, 572, 576, 579, and 582, are shown in Fig. 10.

It can be distinguished from Fig. 10 that at each time instant, there are two red regions, $0° < \theta < 30°$ and $330° < \theta < 360°$, in the surface pressure distribution map, indicating that these two regions of the cylinder surface are under pressure. The rest of the cylinder surface is subjected to suction (in green or blue). This pattern agrees with that of the mean pressure distribution given in Fig. 3(c). Besides, Fig. 10 also provides the spatial variation of C_p at a given time instant. For instance, at time instant $t^* = 565$, the C_p values are low in the region $80° < \theta < 180°$ and $0 < L_Z/D < 5$ shown in Fig. 10(a), which is denoted by a red rectangular box. A local minimum value of C_P is identified to be −1.135, which is at the location of $\theta = 156°$ and $L_Z/D = 2.68$.

Interestingly, it is observed that this local low C_p (or high suction) region shifts to the lower left side at time instant $t^* = 569$, as marked by the red rectangular box in Fig. 10(b). Such a region is found to move to the lower right side in Fig. 10(c) at $t^* = 572$ with respect to that in Fig. 10(b). The same moving pattern of the low C_P (or high suction) region can be identified at the three subsequent time instants in Figs. 10(d)–10(f). The C_p distribution maps shown in Fig. 10 portray the instantaneous flow structure around an imperfectly round circular cylinder with e/D = 4%. A low C_p value indicates a possible existence of a vortex structure in the vicinity of the region. Although there exists several experimental[3,28] and numerical[4] studies investigating the flow structure around a cylinder at various attack angles, the knowledge of the flow structure within the cylinder recirculation zone is still limited. It is worth noting that this local low C_p region is not purely resulted from the von Kármán vortex shedding; otherwise, the entire span should show a similar C_P distribution pattern. We speculate that there might be a unique flow structure that moves along the cylinder axial direction.

Combining Figs. 10(a)–10(f), we can observe that the low C_p (or high suction) region denoted by the red rectangular box in Fig. 10(a) propagates along the axial direction with an "S" pattern. We draw a sketch and use a black dashed line to illustrate how this low C_p (or high suction) region moves along the cylinder span-wise direction in Fig. 10(g). In addition, we utilize the red cross to indicate the geometric center point of the red rectangular box in Figs. 10(a)–10(f). If we estimate the moving speed of the "S" pattern along the cylinder axial direction using the geometric centers of the regions enclosed by the red rectangular box in Figs. 10(b) and 10(c), and the time lag between the time instants associated with these two figures, this speed is determined to be 1.25 m/s. On the other hand, the free-stream velocity component in the cylinder span-wise direction is 1.17 m/s. The agreement on these two speeds strongly suggests that the "S" pattern shown on the pressure coefficient maps is strongly related to the near-wake flow along the cylinder axial direction. In Sec. III B 4, we will examine this unique flow structure using flow visualization techniques in detail.

4. Particle trajectory

To further study the "S" pattern movement of the low C_P (or high suction) region observed in Fig. 10 and discussed in Sec. III B 3, the flow structure surrounding a cylinder in the case corresponding to Fig. 8(f) is visualized by the trajectory of a massless particle. The origin of the selected particle is at $x = 1.7562D$, $y = -0.8889D$, and $z = 4.6911D$. To illustrate how the flow structure evolves in time, we pick three non-dimensional time stamps, $t^* = 565$, 569, and 572, in Fig. 11, which correspond to the time stamps shown in Figs. 10(a)–10(c), respectively. To clearly display the three-dimensional flow structure, three different views are used to capture the particle trajectory in Fig. 11. Figures 11(a), 11(d), and 11(g) show the leeward side view of the particle movement, whereas Figs. 11(b), 11(c), 11(e), 11(f), 11(h), and 11(i) provide two additional views, respectively, from the right and the left side of the cylinder by assuming that the observer faces the oncoming flow. These surfaces are denoted in red at the top of each column of subplots in Fig. 11. To have a better view of the suction force variation on the leeward side of the cylinder, the range of the color map used for illustrating surface pressure distribution is set to correspond to a pressure coefficient variation from −0.7 to 0.

It can be seen from Fig. 11 that the trajectory of the selected particle follows a wavy path winding around the base point (or $\theta = 180°$ in Fig. 4). Clearly, this wavy path has a three-dimensional characteristic, which suggests that the motion of the studied

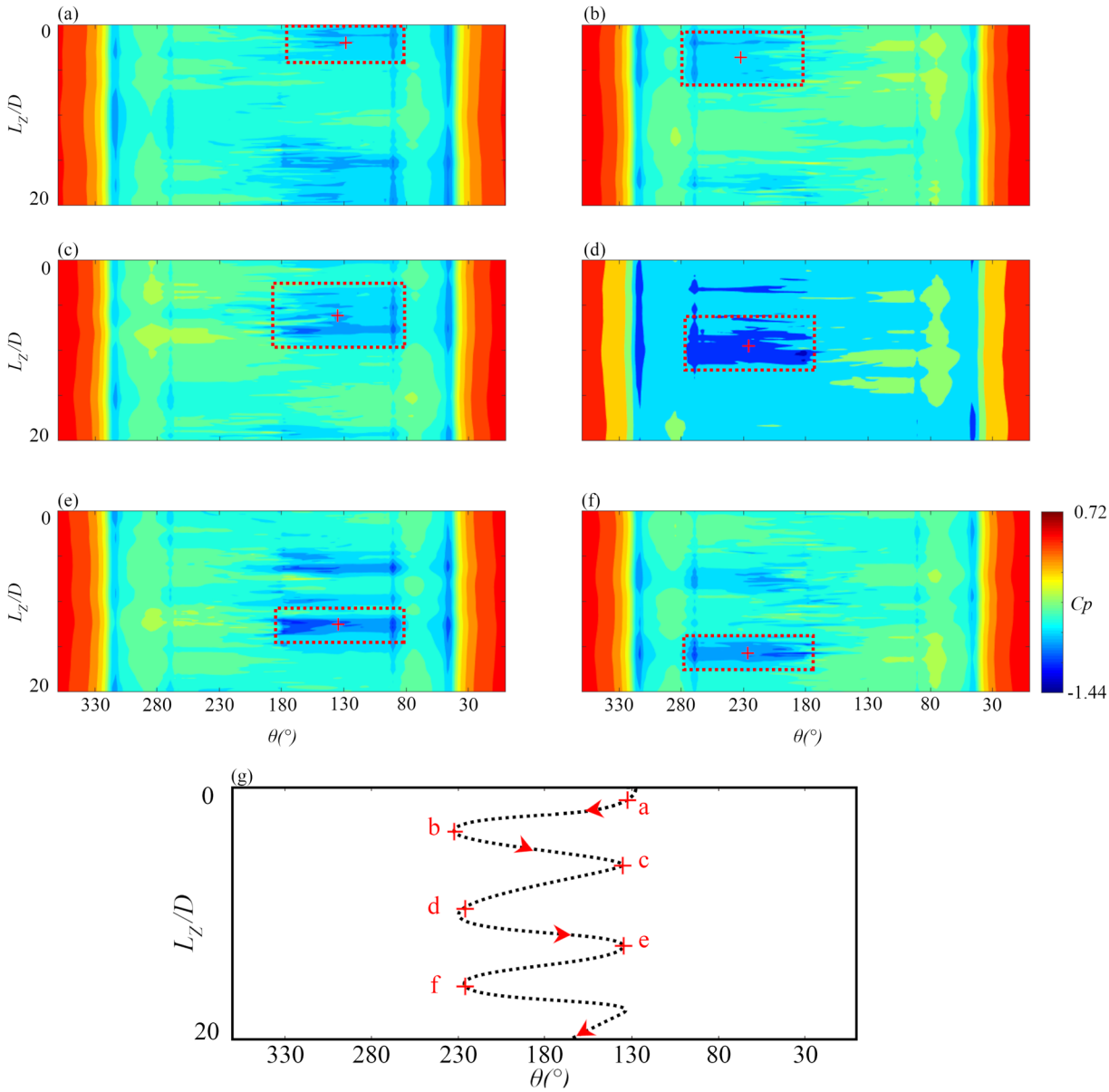

FIG. 10. Surface pressure contour for the case e/D = 4% at Re = 10^4 at non-dimensional time instants t^*: (a) 565, (b) 569, (c) 572, (d) 576, (e) 580, and (f) 583; and (g) a schematic diagram illustrating the trajectory of a high suction region.

particle can be decomposed into two components, with one being tangent to the cylinder circumference and the other along the cylinder axis.

As shown in Figs. 11(a), 11(d), and 11(g), a localized dark blue region appears at different locations of the cylinder surface as time goes by. This dark blue region indicates where the instantaneous low C_P (or high suction) occurs and thus the presence of a vortex structure. Assume an observer stands in the cylinder wake and faces the oncoming flow, then it can be seen that this instantaneous low C_P (or high suction) zone moves from the right side of the cylinder leeward surface at t^* = 565 to the left side at t^* = 569 and swings back again to the right side at t^* = 572. The relocation of this low C_P (or high suction) zone at t^* = 565, 569, and 572 is shown more clearly in Figs. 11(b), 11(f), and 11(h) using the two additional views from the right and the left side of the cylinder. Since the studied particle would be "pulled" toward the high suction zone, it would thus be "pulled" toward the right leeward side of the cylinder surface at t^* = 565, then toward the left at t^* = 569, and so on, i.e., the particle

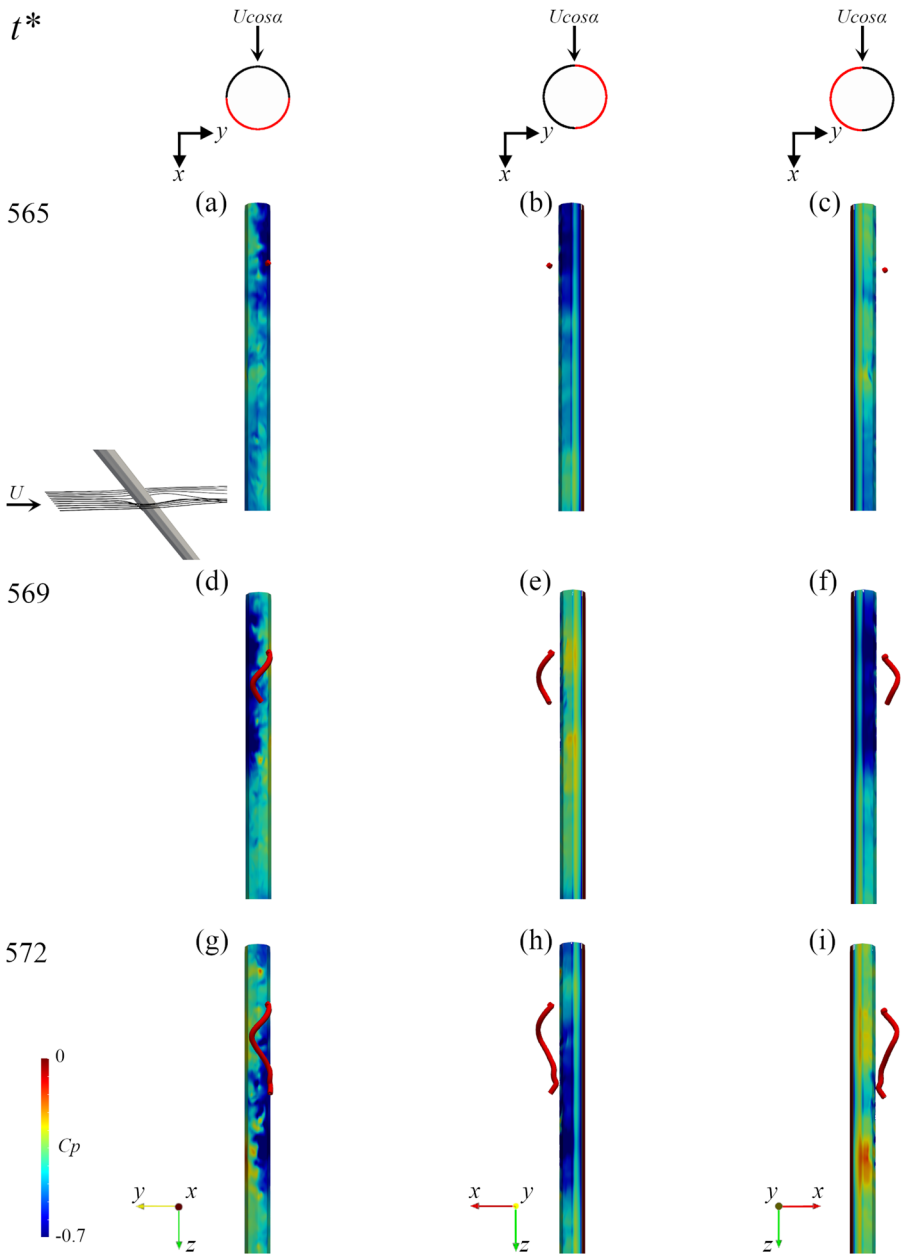

FIG. 11. Particle trajectory of the case e/D = 4% at an attack angle of 45° at Re = 10^4: [(a)–(c)] at t^* = 565, [(d)–(f)] at t^* = 569, and [(g)–(i)] at t^* = 572; the surface pressure coefficient on the cylinder is also contour from −0.7 to 0; the region of the contour in each column is denoted by the red curve of the circle on the top of each column.

would continuously alternate its motion direction along the tangent of the cylinder circumference. Based on the time interval between Figs. 11(a) and 11(g), which is T^* = 7, it can be deduced that the non-dimensional oscillating frequency of the tangential movement of the particle is about 0.143, which agrees well with the Strouhal number of 0.147 obtained earlier for this case (Table II). This implies that the tangential component of the observed wavy motion of the studied particle or the "S" pattern movement of the low C_P (or high suction) region is induced by the formation and shedding of the von Kármán vortices.

The axial component of the particle motion is related to the secondary flow on the leeward side of the cylinder surface. To better illustrate the formation of this secondary flow, we use the stream-trace visualization technique to capture the surrounding flow structure, as shown in Fig. 12(a). It is observed that when the flow approaches and passes the cylinder at a non-zero attack angle, at any arbitrary cross section of the cylinder, part of the flow is trapped within the recirculation zone, which is indicated by the black arrow A in Fig. 12(a). Subsequently, the trapped flow travels downward along the cylinder axial direction. As an accumulating effect of such

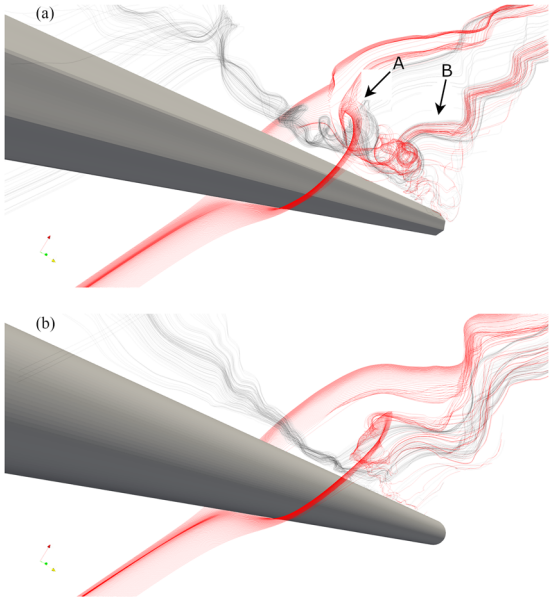

FIG. 12. Instantaneous stream-trace of the studied cases at an attack angle of 45° at $Re = 10^4$: (a) $e/D = 4\%$ and (b) $e/D = 0$.

a downward flow component from all the sections along the cylinder span, a strong secondary flow is formed, which is often referred to as the axial flow.[3] The presence of this secondary axial flow would "push" the flow around the leeward side of the cylinder surface and that in the near-wake to move along the cylinder axial direction. Thus, as time progresses, the low C_P (or high suction) region would not only alternate its location along the tangential direction of the cylinder circumference but also continuously travel along the cylinder axial direction, which leads to the formation of a unique flow structure that moves in an "S" pattern in the cylinder near-wake, as shown in Figs. 10 and 11.

Besides, it is observed that this newly formed axial flow is not stable. Instead of remaining in the recirculation zone while moving along the cylinder axial direction, it would "escape" after a short while by forming vortices and shedding from the cylinder surface. The formation and shedding of the axial vortices would interact with other flow structures, i.e., the von Kármán vortices, in the near-wake and continue to travel farther downstream to the far-wake region. The "escaped" axial flow or the shedded axial vortex is designated by the black arrow B in Fig. 12(a).

For comparison, we also calculate the stream-trace for the perfectly round circular cylinder case, portrayed in Fig. 12(b). Although the formation of the axial flow and the shedding of the axial vortex have also been identified, compared to the case of $e/D = 4\%$ [Fig. 12(a)], the detached shear layer of a perfectly round circular cylinder is found to be farther away from the cylinder surface. This phenomenon can also be inferred from Fig. 7(c) of which in the normal flow case, when $e/D = 4\%$, it has the shortest recirculation length, while that of the perfectly round circular cylinder is the longest. This implies that the presence of the roundness imperfection of a circular cylinder would allow retaining the secondary axial flow in the recirculation zone for a longer time and thus enhance its strength before shedding.

The characteristics of the "S" pattern movement of the low C_P (or high suction) region has been discussed earlier in Sec. III B 4. To further investigate how this unique flow feature would affect aerodynamics of an imperfectly round circular cylinder, a comparison has been made between the flow structure around such a geometrically imperfect circular cylinder with $e/D = 4\%$ at an attack angle of 45° over the time duration with and without the presence of the "S" pattern. Figure 13(a) presents the sectional lift coefficient contour of the studied cylinder along the z-axis during $467 < t^* < 606$, whereas Fig. 13(b) gives a zoomed-in view of the sectional C_L contour when $565 < t^* < 592$, which includes the six time instants discussed in Sec. III B 3. As shown in Figs. 13(a) and 13(b), the moving pattern of the red/blue strips during $t^* = 565$ and 588, as marked by a white elliptical ring (denoted by E5) in Figs. 13(a) and 13(b), forms a complete "S" pattern movement of the low C_P (or high suction) region when it travels from one cylinder end to the other. If we draw a horizontal line at an arbitrary span-wise location of the cylinder in Fig. 13(b), a continuous alternating pattern of the color between blue (or cyan) and red (or yellow) can be observed, which, according to the color map, represents the presence of the alternating sectional lift direction at that specific location. This alternating pattern of the sectional lift direction results from the shedding of the conventional von Kármán vortex. Besides, another phenomenon can also be observed, which is denoted by a white elliptical ring in Fig. 13(a) where the absolute value of the sectional lift within a short time duration becomes much larger than those in the neighboring regions. This amplification of sectional C_L occurs intermittently, as indicated by the repeated appearance of the red/blue stripe bundle in Fig. 13(a) as time goes by. The same phenomenon has been noted in Fig. 8(f) and discussed in Sec. III B 1. Nevertheless, as has been pointed out earlier, the time interval between the two adjacent bundles of red/blue stripes is multiple times of the time duration of a conventional von Kármán vortex shedding. It is roughly five times (time lag between E1 and E2) in Fig. 8(f) and ten times (time lag between E3 and E4) in Fig. 13(a). This would lead to an intermittent amplification of the sectional lift at a frequency much lower than that of the von Kármán vortex shedding. Naturally, the question then is what causes this intermittent amplification pattern of the sectional lift?

To clarify the underlying mechanism, the flow structure at the cylinder span-wise location of $L_z/D = 4.69$ is further explored for the time instants with and without the occurrence of intermittent sectional lift amplification. A horizontal plane is introduced along the same direction as the free-stream velocity and intercepts the cylinder at $L_z/D = 4.69$, as shown schematically at the left bottom corner of Fig. 13(c). The vorticity component within this plane is calculated by the dot product of the vorticity vector and the normal vector of the plane. It ranges from $-100\ s^{-1}$ to $100\ s^{-1}$ and can be utilized to interpret the formation of vortices in the cylinder wake. Besides, the stream-trace technique is applied to visualize the three-dimensional flow structure.

The characteristics of the flow field, associated with the four von Kármán vortex shedding events, will be discussed in detail. They occur at time instants $t^* = 570$, 573, 586, and 589 and are designated by letters A, B, C, and D, respectively, in Fig. 13(b). Among the four, events A and B occur within the bundle of the red/blue stripes when

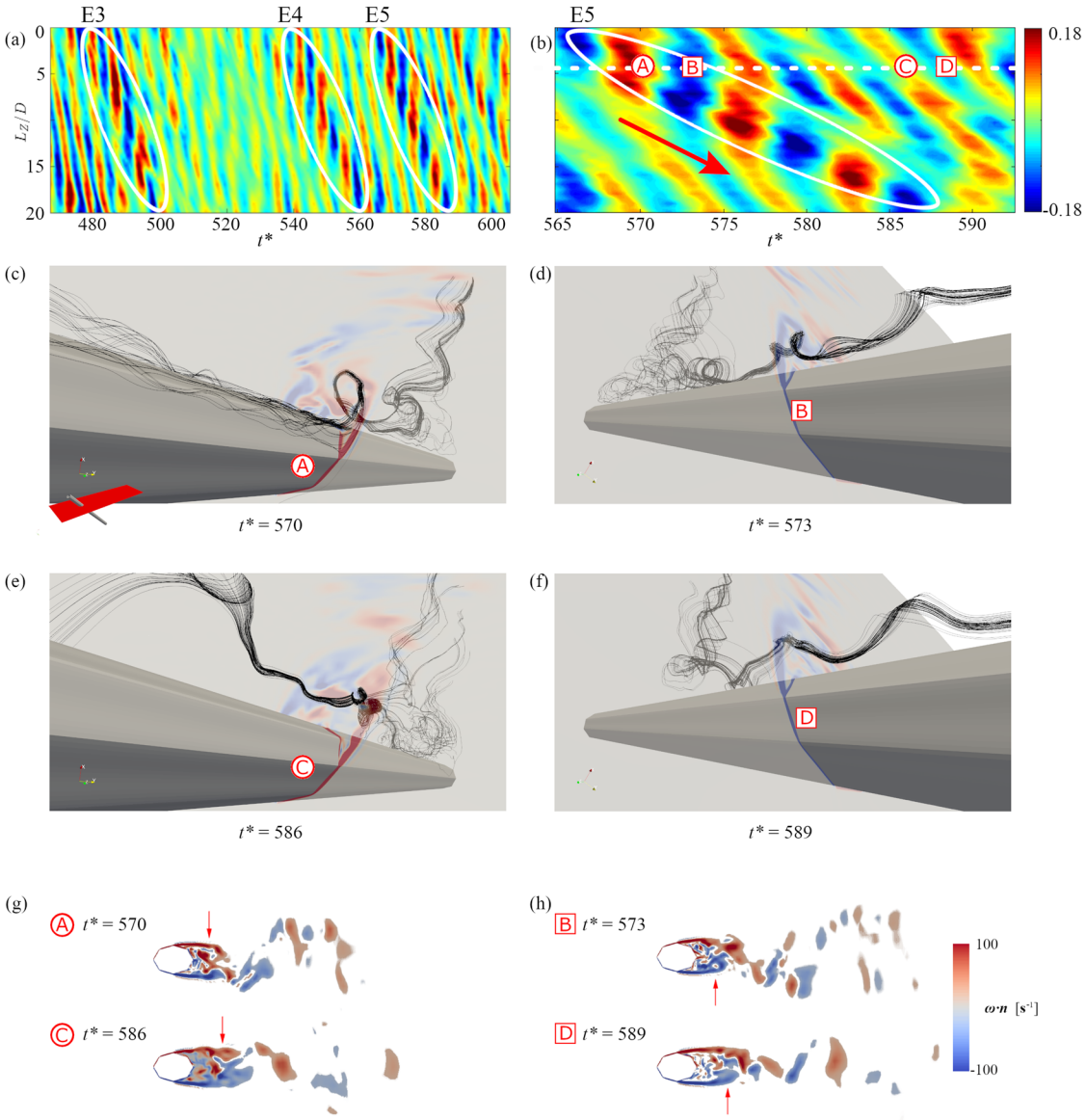

FIG. 13. Illustration of the mechanism of the moving force pattern observed in the contour of sectional C_L: (a) the time history from $467 < t^* < 606$; (b) a zoomed-in view on the time history $565 < t^* < 592$; the flow structure at (c) $t^* = 570$, (d) $t^* = 573$, (e) $t^* = 586$, and (f) $t^* = 589$; and contours of the vorticity component (g) $t^* = 570$ and 586, and (h) $t^* = 573$ and 589.

the sectional lift is amplified. If we assume that the observer stands upstream of the cylinder and faces it, then one will see the shedding of the von Kármán vortex from the right side of the cylinder in events A and C and from the left side of the cylinder in events B and D. To distinguish the shedding side of the von Kármán vortex, letters A and C are enclosed in a circle box, whereas letters B and D are enclosed in a square. Figures 13(c), 13(e), and 13(g) portray the respective stream trace and vorticity component in the plane $L_z/D = 4.69$ for events A and C of which the rolling shear layer is shown in red, whereas those associated with events B and D are illustrated in Figs. 13(d), 13(f), and 13(h) with the rolling shear layer shown in blue.

Comparing the stream-trace of events A and B in Figs. 13(c) and 13(d) with that of events C and D in Figs. 13(e) and 13(f), it can be seen that the axial flow in events A and B stays very close to the cylinder leeward side surface. At the time instant of $t^* = 570$ and 573, the axial flow rolls up and forms vortex. Furthermore, the proximity of the axial flow to the cylinder surface allows it to entrain more flow from the cylinder near-wake during the axial vortex formation process and leaves a region with higher suction. This renders

the rolling up of the shear layer from the cylinder side to be drawn closer to its leeward surface. This is clearly reflected in Figs. 13(g) and 13(h) of which the vortex core of events A and B, as indicated by the red arrow, located closer to the cylinder leeward surface when compared with those in events C and D. Therefore, when a conventional von Kármán vortex is formed and shedded, more flow would be entrained from the cylinder near-wake and leads to a further increase in the suction. The combined effect of the axial vortex and von Kármán vortex formation and shedding would then result in a much larger transverse lift due to higher suction on the leeward side of the cylinder surface, i.e., the amplification of the lift. For events C and D, however, since the axial flow is not closely attached to the cylinder surface, its formation would have much less impact on the flow in the cylinder near-wake as well as on the formation location of the von Kármán vortex [Figs. 13(g) and 13(h)] and thus the transverse lift on the cylinder.

It has been pointed out in Secs. III A 3 and III B 4 and also shown in Figs. 7(c) and 12 that, compared to a perfectly round circular cylinder, an imperfectly round one would have a shorter recirculation length and would be able to retain more axial flow closer to the cylinder leeward surface. The intensified axial flow, when rolls up, would generate a stronger axial vortex and promote the entrainment of more flow from the cylinder near-wake. As explained earlier, the interaction between the formation of the axial vortex and conventional von Kármán vortex would result in an enhanced transverse lift. Since the frequency of axial vortex formation is a few times lower than that of the von Kármán vortex, the transverse lift acting on an imperfectly round circular cylinder would be amplified intermittently.

Stay cables on real cable-stayed bridges could have the roundness imperfection of their cross-sectional shape caused by various factors including manufacturing process, assemblage, shipping, and storage. This could considerably alter the surrounding flow field and form a unique flow structure similar to that observed in the current study. The imperfect roundness in a real cable could cause an interaction between the axial vortex and the conventional von Kármán vortex, which would amplify the transverse lift intermittently. This could ultimately develop into an excitation source to trigger large-amplitude or even divergent cable motion, such as dry inclined cable galloping.

It should be pointed out that the flow pattern observed in the current study is different from the trailing edge vortex behind a curved cylinder. For example, Gallardo *et al.*[29] studied a curved cylinder using LES and they observed a swirling pattern. In their study, those swirling structures formed on both sides of the cylinder and there were no interactions between them. The scale of the "S" pattern observed in the current study is larger than the swirling structure documented by Gallardo *et al.*[29] The current particle trajectory shows that the flow moves back and forth between the two sides of the cylinder around the leeward base point, whereas the swirling structures never crossed the centerline, as shown in Fig. 5(b) of their paper.

IV. CONCLUDING REMARKS

The impact of the roundness imperfection in the cross-sectional shape of a circular cylinder on its neighboring flow structure and the associated aerodynamic forces has been numerically scrutinized using delayed detached eddy simulation at a Reynolds number of 10^4 and an attack angle of 0° or 45°. Four levels of roundness imperfection, represented by the roundness ratio e/D = 0%, 1%, 4%, and 10%, respectively, have been investigated. The surface pressure distribution, the aerodynamic forces, and the wake structure have been examined in detail. Results show that compared to a perfectly round circular cylinder, the presence of roundness imperfection could have a considerable impact on the surrounding flow structure and cause a subsequent influence on the surface pressure and the aerodynamic forces.

In the normal flow condition, the cylinder mean surface pressure distribution is found to be sensitive to the change in the roundness of the cross section. Although for a small imperfection of e/D = 1%, $\overline{C_P}$ closely follows the distribution pattern of a perfectly round circular cylinder, with the increase in e/D, $\overline{C_P}$ increases monotonically on the cylinder windward surface. This monotonicity fades on the leeward side, where the minimum $\overline{C_P}$ is observed to occur in the case of e/D = 4%. The roundness imperfection has a nonlinear effect on the size of the recirculation zone, with that of the perfectly round circular cylinder being the largest and the one with e/D = 4% being the smallest. However, the presence of roundness imperfection has a negligible influence on the span-wise synchronization of von Kármán vortex formation and shedding.

When the flow approaches a circular cylinder at an attack angle of 45°, a unique tilted and moving pattern of the yellow/cyan (or red/blue) stripes representing the von Kármán vortices is observed on the sectional C_L contour, with the occurrence of a larger sectional lift (red/blue stripes) gradually shifting from one end of the cylinder to the other as time goes by. From the instantaneous C_P distribution contour, the location of the low C_P (or high suction) zone is observed to vary with time and move in an "S" pattern. The current study found that the presence of the roundness imperfection could induce the formation of a stronger axial vortex and its interaction with the conventional von Kármán vortex to intermittently amplify the transverse lift acting on the cylinder. In the current study, the strongest interaction is found in the case of e/D = 4% where several incidents of sectional transverse lift amplification are captured during a short period of time. Considering the fact that real bridge stay cables on site also have the issue of roundness imperfection in their cross-sectional shape, it is therefore speculated that this geometric imperfection would similarly introduce an intermittently amplified transverse lift to a cable and trigger aerodynamically unstable or even divergent motion, such as the dry inclined cable galloping.

ACKNOWLEDGMENTS

The authors are grateful to the Natural Sciences and Engineering Research Council of Canada (NSERC) for supporting this project. This work was made possible by mp2 from Université de Sherbrooke, managed by Calcul Québec and Compute Canada; the operation of this supercomputer was funded by the Canada Foundation for Innovation (CFI), the ministère de l'Économie, de la science et de l'innovation du Québec (MESI), and the Fonds de recherche du Québec – Nature et technologies (FRQ-NT).

REFERENCES

[1]S. Cheng, G. L. Larose, M. G. Savage, and H. Tanaka, "Aerodynamic behaviour of an inclined circular cylinder," Wind Struct. **6**, 197–208 (2003).

[2]J. B. Jakobsen, T. L. Andersen, J. H. G. Macdonald, N. Nikitas, G. L. Larose, M. G. Savage, and B. R. McAuliffe, "Wind-induced response and excitation characteristics of an inclined cable model in the critical Reynolds number range," J. Wind Eng. Ind. Aerodyn. **110**, 100–112 (2012).

[3]M. Matsumoto, T. Yagi, H. Hatsuda, T. Shima, M. Tanaka, and H. Naito, "Dry galloping characteristics and its mechanism of inclined/yawed cables," J. Wind Eng. Ind. Aerodyn. **98**, 317–327 (2010).

[4]D. Yeo and N. P. Jones, "Investigation on 3-D characteristics of flow around a yawed and inclined circular cylinder," J. Wind Eng. Ind. Aerodyn. **96**, 1947–1960 (2008).

[5]W. Cheng, D. I. Pullin, R. Samtaney, W. Zhang, and W. Gao, "Large-eddy simulation of flow over a cylinder with Re_D from 3.9×10^3 to 8.5×10^5: A skin-friction perspective," J. Fluid Mech. **820**, 121–158 (2017).

[6]G. L. Larose, S. McTavish, H. Bosch, S. Stoyanoff, J. B. Jakobsen, and J. Wang, "Wind tunnel tests on free to respond bridge stay cable models," in *International Symposium on the Dynamics and Aerodynamics of Cables* (Clássica, Artes Gráficas, 2017), pp. 103–110.

[7]D. R. Johnstone, A. E. Potts, H. Marcollo, and P. Kurts, "Drilling riser case studies comparing the drag performance of LGS technology to convential bouyanct units and fairings," in *International Conference on Ocean, Offshore and Arctic Engineering* (American Society of Mechanical Engineers, New York, NY, 2017).

[8]H. Marcollo, A. Potts, D. Johnstone, P. Pezet, and P. Kurts, "Drag reduction and VIV suppression behaviour of LGS technology integral to drilling riser buoyancy units," in *International Conference on Ocean, Offshore and Arctic Engineering* (American Society of Mechanical Engineers, New York, NY, 2016), p. V002T08A075.

[9]S. Raayai-Ardakani and G. H. McKinley, "Drag reduction using wrinkled surfaces in high Reynolds number laminar boundary layer flows," Phys. Fluids **29**, 093605 (2017).

[10]N. Yadav, S. W. Gepner, and J. Szumbarski, "Instability in a channel with grooves parallel to the flow," Phys. Fluids **29**, 084104 (2017).

[11]A. Mohammadi and J. M. Floryan, "Groove optimization for drag reduction," Phys. Fluids **25**, 113601 (2013).

[12]M. M. Zdravkovich, *Flow Around Circular Cylinders Vol. 1: Fundamentals* (Oxford University Press, New York, 1997).

[13]W. Cheng, D. I. Pullin, and R. Samtaney, "Large-eddy simulation of flow over a grooved cylinder up to transcritical Reynolds numbers," J. Fluid Mech. **835**, 327–362 (2018).

[14]A. Benidir, O. Flamand, L. Gaillet, and G. Dimitriadis, "Impact of roughness and circularity-defect on bridge cables stability," J. Wind Eng. Ind. Aerodyn. **137**, 1–13 (2015).

[15]J. Wang, J. B. Jakobsen, S. McTavish, and G. L. Larose, "Aerodynamic performance of a grooved cylinder in flow conditions encountered by bridge stay cables in service," J. Wind Eng. Ind. Aerodyn. **188**, 80–89 (2019).

[16]S. Cheng, G. L. Larose, M. G. Savage, H. Tanaka, and P. A. Irwin, "Experimental study on the wind-induced vibration of a dry inclined cable-Part I: Phenomena," J. Wind Eng. Ind. Aerodyn. **96**, 2231–2253 (2008).

[17]H. G. Weller, G. Tabor, H. Jasak, and C. Fureby, "A tensorial approach to computational continuum mechanics using object-oriented techniques," Comput. Phys. **12**, 620–631 (1998).

[18]U. Piomelli, "Wall-layer models for large-eddy simulations," Prog. Aerosp. Sci. **44**, 437–446 (2008).

[19]F. R. Menter and M. Kuntz, "Adaptation of eddy-viscosity turbulence models to unsteady separated flow behind vehicles," in *The Aerodynamics of Heavy Vehicles: Trucks, Buses, and Trains* (Springer Berlin Heidelberg, 2004), pp. 339–352.

[20]R. Wang, S. Cheng, and D. S.-K. Ting, "Effect of yaw angle on flow structure and cross-flow force around a circular cylinder," Phys. Fluids **31**, 014107 (2019).

[21]P. R. Spalart, S. Deck, M. L. Shur, K. D. Squires, M. K. Strelets, and A. Travin, "A new version of detached-eddy simulation, resistant to ambiguous grid densities," Theor. Comput. Fluid Dyn. **20**, 181 (2006).

[22]R. Wang, S. Cheng, and D. S.-K. Ting, "Simulating the role of axial flow in stay cable vibrations via a perforated wake splitter plate," in *Wind Engineering in Natural Hazards* (ASCE Special Edition, 2017), pp. 111–132.

[23]R. Wang, "Numerical simulations on flow around an inclined circular cylinder at high Reynolds number," M.S. thesis, University of Windsor, 2018.

[24]A. Roshko, "On the development of turbulent wakes from vortex streets," NACA Technical Report No. 1191, 1954.

[25]C. Norberg, "Pressure forces on a circular cylinder in cross flow," in *IUTAM Symposium on Bluff Body Wakes, Dynamics and Instabilities*, edited by H. Eckelmann, J. M. R. Graham, P. Huerre, and P. A. Monkewitz (Springer Berlin Heidelberg, Berlin, Heidelberg, 1993), pp. 275–278.

[26]G. Schewe, "On the force fluctuations acting on a circular cylinder in crossflow from subcritical up to transcritical Reynolds numbers," J. Fluid Mech. **133**, 265–285 (1983).

[27]V. de Ville de Goyet, "Aerodynamic behaviour of cables at third Bosphorus bridge - observation on site," in *International Symposium on the Dynamics and Aerodynamics of Cables* (Clássica, Artes Gráficas, 2017), pp. 53–71.

[28]M. Y. Younis, M. M. Alam, and Y. Zhou, "Flow around two non-parallel tandem cylinders," Phys. Fluids **28**, 125106 (2016).

[29]J. P. Gallardo, H. I. Andersson, and B. Pettersen, "Turbulent wake behind a curved circular cylinder," J. Fluid Mech. **742**, 192–229 (2014).

[30]A. Travin, M. Shur, M. Strelets, and P. Spalart, "Detached-eddy simulations past a circular cylinder," Flow, Turbul. Combust. **63**, 293–313 (1999).

[31]P. D. Weidman, "Wake transition and blockage effects on cylinder base pressures," Ph.D. thesis, California Institute of Technology, 1968.

[32]S. Dong, G. E. Karniadakis, A. Ekmekci, and D. Rockwell, "A combined direct numerical simulation-particle image velocimetry study of the turbulent near wake," J. Fluid Mech. **569**, 185–207 (2006).

[33]C. Norberg, "LDV-measurements in the near wake of a circular cylinder," ASME Paper No. FEDSM98-521, 1998.